Article:
Sheldon, S.J., Brash, A.J., Skolnick, M.S. et al. (2024) Optical spin initialization and readout with a cavity-coupled quantum dot in an in-plane magnetic field. Physical Review B, 110. 235411. ISSN: 2469-9950

https://doi.org/10.1103/physrevb.110.235411

Optical spin initialization and readout with a cavity-coupled quantum dot in an in-plane magnetic field

Samuel J. Sheldon,[1] Alistair J. Brash,[1] Maurice S. Skolnick,[1] A. Mark Fox,[1] and Jake Iles-Smith[1,2]
[1]*School of Mathematical and Physical Sciences, University of Sheffield, Sheffield S3 7RH, United Kingdom*
[2]*Department of Physics and Astronomy, The University of Manchester, Oxford Road, Manchester M13 9PL, United Kingdom*

(Received 28 June 2022; revised 5 October 2024; accepted 22 November 2024; published 10 December 2024)

The spin of a charged semiconductor quantum dot (QD) coupled to an optical cavity is a promising candidate for high-fidelity spin-photon interfaces; the cavity selectively modifies the decay rates of optical transitions such that spin initialization, manipulation, and readout are all possible in a single magnetic field geometry. By performing cavity QED calculations, we show that a cavity with a single, linearly polarized mode can simultaneously support both high-fidelity optical spin initialization and readout in a single, in-plane (Voigt geometry) magnetic field. Furthermore, we demonstrate that single-mode cavities always outperform bimodal cavities in experimentally favorable driving regimes. Our analysis, when combined with established methods of control in a Voigt geometry field, provides optimal parameter regimes for high-fidelity initialization and readout, and coherent control in both cavity configurations, providing insights for the design and development of QD spin-photon interfaces as the basis of quantum network nodes and for the generation of photonic graph states.

DOI: 10.1103/PhysRevB.110.235411

I. INTRODUCTION

Experiments have demonstrated that the spin states of single electrons confined to quantum dots (QDs) are long lived [1,2], with coherence times exceeding μs [3,4], making them promising candidates for an efficient light-matter interface [5]. Furthermore, quantum logic gates may be implemented on ps timescales using ultrafast optical manipulation of spin states [3]. Combined, these disparate timescales allow many gate operations to be performed within a single lifetime of the charge state. However, for spin-photon interfaces to be used in optical quantum technologies, such as the efficient generation of entangled photonic graph states [6–13] and spin-photon logic [14,15] required for many long-range secure quantum network protocols [16,17], it is necessary to prepare, control, and readout the single-spin states with a high fidelity.

Ordinarily, combining optical spin control and readout requires the use of orthogonal magnetic field geometries: spin control relies on the in-plane Voigt geometry [Fig. 1(a)] to provide an effective coupling between the spin ground states [18], while readout drives a *cyclic transition* [19,20] in an out-of-plane Faraday field to produce a detectable signal, ideally within the "single-shot" limit [21,22]. However, optical spin readout can also be achieved in the Voigt geometry through polarization-dependent Purcell enhancement of the optical transitions introduced by coupling to nanophotonic structures [23–25].

In this work, we investigate the impact of coupling between a single charged QD in a Voigt geometry magnetic field, and a single cavity supporting either one or two confined modes (henceforth referred to as a single-mode or bimodal cavity, respectively), on the spin initialization and readout fidelity. We show that depending on the linewidths and detunings of the cavity modes, a bimodal cavity may enhance all optical transitions present in a Voigt geometry field, reducing the effectiveness of the quasicycling transition. While careful selection of the bimodal cavity parameters may mitigate these effects, the additional enhancement of the QD transitions results in different cavity parameter requirements for initialization and readout. Thus, when coupled to a bimodal cavity, we show there is no single set of cavity parameters that simultaneously results in both a good optical initialization and readout fidelity. Furthermore, we show that single-mode optical cavities outperform bimodal cavities for both optical initialization and optical readout across all studied parameter regimes, and can be used to achieve an optimal fidelity in both stages using a single set of cavity parameters.

The paper is organized as follows: in Sec. II, we introduce the background theory for a charged QD interacting with a single-mode or bimodal cavity. Sections III and IV investigate how the two cavity configurations impact spin initialization and readout, respectively, in isolation. We then discuss the best cavity configurations for initialization and readout in tandem in Sec. V.

II. BACKGROUND THEORY

In the absence of any applied magnetic fields, a single electron confined to a QD possesses a spin degree of freedom with two degenerate ground states $\{|\uparrow\rangle_z, |\downarrow\rangle_z\}$ defined along the QD growth (z) axis, which are chosen to have zero energy. Optically exciting the QD introduces an exciton, forming two negatively charged trion states $\{|\downarrow\uparrow, \Downarrow\rangle_z, |\uparrow\downarrow, \Uparrow\rangle_z\}$ with energy $\hbar\omega_0$. Applying a Voigt geometry magnetic field to the QD

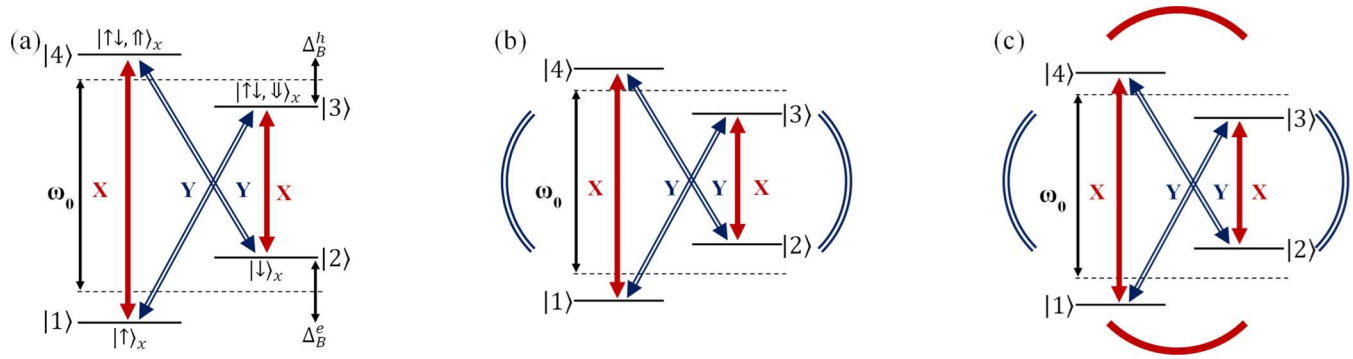

FIG. 1. (a) An energy level diagram of a negatively charged quantum dot (QD) in an applied Voigt geometry magnetic field. The degeneracy of the ground and excited eigenstates, written in the basis along the magnetic field axis parallel to the x axis, is lifted by the Zeeman interaction. All four transitions are equally allowed, leading to the formation of two Λ-systems ($1 \rightarrow 4 \rightarrow 2$ and $2 \rightarrow 3 \rightarrow 1$). The vertical transitions possess the orthogonal linear polarization to the diagonal transitions. (b) A Y-polarized single-mode cavity coupled to the Y-polarized diagonal transitions of a charged QD in a Voigt geometry magnetic field. (c) A bimodal cavity with two orthogonal, linearly polarized cavity modes coupled to a charged QD in a Voigt geometry magnetic field. In (b) and (c), the curved lines indicate the configuration of the cavity mode(s), and the line style (solid or compound) and color indicates the transitions to which the cavity mode couples.

lifts the energy degeneracy of both the ground and excited spin states, splitting them by the Zeeman energies $\Delta_B^e = g_e \mu_B B$ and $\Delta_B^h = g_h \mu_B B$, respectively [Fig. 1(a)]. Here, μ_B is the Bohr magneton, g_e and g_h are the electron and hole effective in-plane g factors, B is the applied magnetic field strength, and we have ignored any diamagnetic shift. For convenience, we redefine the QD spin states in the basis along the magnetic field axis as $\{|1\rangle = |\uparrow\rangle_x, |2\rangle = |\downarrow\rangle_x, |3\rangle = |\downarrow\uparrow, \Downarrow\rangle_x, |4\rangle = |\uparrow\downarrow, \Uparrow\rangle_x\}$. Unless otherwise stated, we assume an applied field of $B = 5$ T, which yields $\Delta_{\mathrm{B}}^{\mathrm{e}}/2\pi = 35$ GHz and $\Delta_{\mathrm{B}}^{\mathrm{h}}/2\pi = 20$ GHz, with $g_{\mathrm{e}} = 0.5$ and $g_{\mathrm{h}} = 0.3$ [26].

In the Voigt geometry, there are four allowed optical transitions with equal magnitude, forming two Λ-systems coupling each excited state to both ground states via two orthogonal, linearly polarized transitions [Fig. 1(a)]. While quasicycling transitions are most easily introduced in the Voigt geometry via coupling to a cavity with a single, linearly polarized mode [27–29] [Fig. 1(b)], there are many photonic structures, such as micropillar cavities [30], point-defect photonic crystal (PhC) cavities [31], crossed nanobeam cavities [32], and open-access microcavities [33], that naturally possess two orthogonal, linearly polarized modes [Fig. 1(c)]. While such bimodal cavities have been used to suppress resonant laser background in QD single-photon sources [33,34], there remain open questions as to the impact on the orthogonally polarized transitions necessary for spin initialization and readout. Thus, in our setup, each of the Λ-systems transitions can occur through coupling to the free electromagnetic vacuum or via an optical cavity. The latter is included in the system Hamiltonian $H_S = H_0 + H_I$, where ($\hbar = 1$)

$$H_0 = \frac{\Delta_{\mathrm{B}}^{\mathrm{e}}}{2}(\sigma_{22} - \sigma_{11}) + \left(\omega_0 - \frac{\Delta_{\mathrm{B}}^{\mathrm{h}}}{2}\right)\sigma_{33} + \left(\omega_0 + \frac{\Delta_{\mathrm{B}}^{\mathrm{h}}}{2}\right)\sigma_{44} + \sum_{\lambda=X,Y} \nu_\lambda a_\lambda^\dagger a_\lambda. \quad (1)$$

Here we have defined the spin operators as $\sigma_{ij} = |i\rangle\langle j|$ and introduced the cavity mode creation (annihilation) operators $a_\lambda^\dagger$ (a_λ) with frequency ν_λ, where $\lambda = X,\ Y$ denotes the polarization of the cavity mode. In physical systems, the degeneracy of the bimodal cavity is often lifted either by intentional design [32,35–37] or by fabrication imperfections [38,39], and we therefore assume the cavity modes are detuned.

Applying the rotating wave approximation to our Hamiltonian, the light-matter interaction takes a Jaynes-Cummings form,

$$H_I = \sum_{\lambda=X,Y} g_\lambda a_\lambda^\dagger \boldsymbol{\sigma}_\lambda + g_\lambda^* a_\lambda \boldsymbol{\sigma}_\lambda^\dagger, \quad (2)$$

where g_λ is the light-matter interaction strength for the relevant cavity mode, and we have introduced the collective transition operators $\boldsymbol{\sigma}_X = \sigma_{14} + \sigma_{23}$ and $\boldsymbol{\sigma}_Y = \sigma_{24} + \sigma_{13}$ [Fig 1(c)]. With the above definitions, we can recover the single Y-polarized mode cavity setup depicted in Fig. 1(b) by setting $g_X = \nu_X = 0$.

Spin initialization and readout necessitate coherent driving of the spin and cavity degrees of freedom, respectively. This is included semiclassically in the model via time-dependent driving terms with frequency ω_l. This leads to a total Hamiltonian of the form $H_T(t) = H_0 + H_I + H_D^{QD}(t) + H_D^C(t)$, where, in the dipole and rotating wave approximations, the QD driving term may be written as

$$H_D^{QD}(t) = -\frac{1}{2}\sum_{\lambda=X,Y} \Omega_\lambda(t) e^{i\omega_l t}\boldsymbol{\sigma}_\lambda + \mathrm{H.c.} \quad (3)$$

Here, $\Omega_\lambda(t)$ is the time-dependent Rabi frequency for the relevant polarization mode. Direct excitation of the QD occurs when the excitation laser is spatially or spectrally decoupled from the cavity mode(s). That is when the laser is orientated orthogonally to the cavity axes or far detuned from the cavity resonance. The cavity-driving Hamiltonian takes a similar form to the direct QD excitation Hamiltonian,

$$H_D^C(t) = -\sum_{\lambda=X,Y} \epsilon_\lambda(t) e^{i\omega_l t} a_\lambda + \mathrm{H.c.}, \quad (4)$$

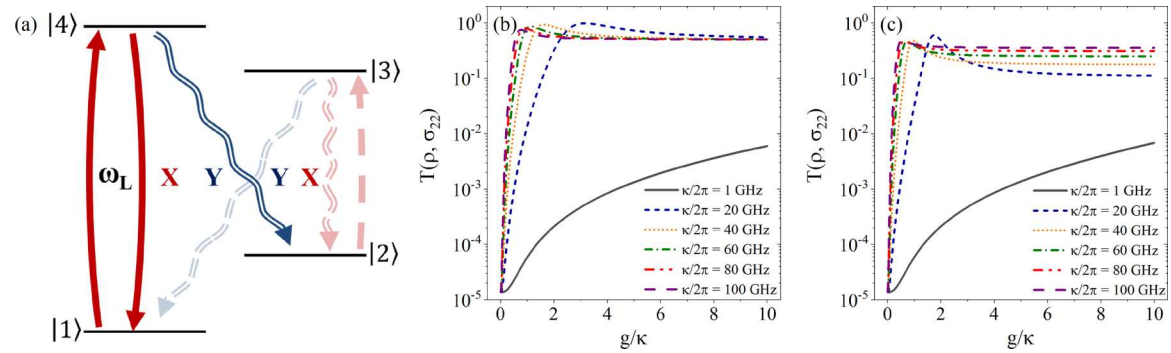

FIG. 2. (a) A schematic of the initialization process. The $|1\rangle \rightarrow |4\rangle$ transition is coherently driven on resonance $[\omega_l = \omega_0 + (\Delta_B^e + \Delta_B^h)/2]$ transferring the spin population to $|2\rangle$ via the $|4\rangle \rightarrow |2\rangle$ transition. Off-resonant driving of the $|2\rangle \rightarrow |3\rangle$ transition returns the spin population to $|1\rangle$. (b), (c) The trace distance between the system steady state after the initialization process and the $|2\rangle$ ground state as a function of g/κ when coupled to a Y-polarized single-mode cavity and a bimodal cavity, respectively. Parameters: $B = 5$ T, $g_{e(h)} = 0.5(0.3)$, $\gamma^{-1} = 1$ ns, $\Omega_X/2\pi = 10^{-3}$ GHz, $\nu_X = \omega_0$, and $\nu_Y = \omega_0 + (\Delta_B^h - \Delta_B^e)/2$.

where $\epsilon_\lambda(t)$ is the time-dependent cavity-driving strength. Optical excitation via a cavity mode occurs when the excitation laser is spatially coupled to the mode and spectrally near the cavity resonance. For convenience, we work in a rotating frame with respect to the laser frequency ω_l.

During spin initialization, the two excitation schemes defined here are qualitatively equivalent, with the only difference being the required excitation power. Here we only consider optical initialization via direct excitation to enable a fair comparison between the cavity configurations. On the other hand, optical readout directly probes the properties of the cavity mode and thus requires cavity driving.

In addition to the unitary dynamics generated by the Hamiltonian $H_T(t)$, there are also loss processes acting on the cavity-QD system, namely, the emission of photons via the cavity or the electromagnetic vacuum. These are accounted for through a standard Lindblad master equation of the form [40]

$$\frac{\partial \rho(t)}{\partial t} = -i[H_T(t), \rho(t)] + \sum_{\lambda=X,Y} \frac{\kappa_\lambda}{2}\mathcal{L}_{a_\lambda}[\rho(t)] + \frac{\gamma_\lambda}{2}\mathcal{L}_{\sigma_\lambda}[\rho(t)], \quad (5)$$

where $\rho(t)$ is the reduced density matrix of the cavity-QD system, and $\mathcal{L}_O[\rho] = 2O\rho O^\dagger - \{O^\dagger O, \rho\}$ is the Lindblad superoperator. Equation (5) captures the emission of photons in a given polarization state λ via two different channels: the first is leakage from the cavity mode, occurring with a rate κ_λ, and the second is spontaneous emission directly from the four-level system (4LS) with rate γ_λ. Throughout this paper, we shall assume that both polarization transitions have the same lifetime, such that $\gamma_{\lambda=X,Y}^{-1} = \gamma^{-1} = 1$ ns, and in the bimodal case we assume that the cavity modes have identical linewidths ($\kappa_{\lambda=X,Y} = \kappa$) such that $|g_{X,Y}| = |g|$ ($g_X = g$, $g_Y = ig$). The effects of pure dephasing are considered in the Appendix and are shown to be negligible in most cases. All calculations presented in this paper were performed using the PYTHON package QUTIP [41].

III. SPIN INITIALIZATION

Assuming an initial state with $\rho_{jj} = 0.5$ for $j \in \{1, 2\}$ and $\rho_{ij} = 0$ otherwise, we wish to prepare the system in the spin state $|2\rangle$ using the protocol presented in [42,43] and illustrated in Fig. 2(a). Initialization is achieved by resonantly driving the $|1\rangle \rightarrow |4\rangle$ transition using an X-polarized laser (i.e., $\Omega_X > 0$, $\Omega_Y = 0$), such that $\omega_l = \omega_0 + (\Delta_B^e + \Delta_B^h)/2$. The state $|2\rangle$ is then populated by the $|4\rangle \rightarrow |2\rangle$ transition. We choose to initialize the spin state by driving the X-polarized transitions owing to the larger detuning between the transitions relative to the laser bandwidth, minimizing the off-resonant processes that induce unwanted spin flips away from the $|2\rangle$ target state.

To quantify the initialization fidelity, we use the trace distance, $T(\rho, \varrho) = \frac{1}{2}\mathrm{Tr}\sqrt{(\rho - \varrho)^2}$, between the prepared ($\rho$) and target ($\varrho$) states [44]. The trace distance provides a measure of the distinguishability of two given states using the entirety of the density matrix including all state populations and coherences. For the pure target state used in this case ($\varrho = \sigma_{22}$), this definition is equivalent to the fidelity used in other studies [25,26,45]. Here we choose to quantify the success of the initialization process using the more general trace distance, as this is often simpler to calculate and provides a true metric on density matrix space, naturally distinguishing between coherent superposition and mixed spin states which would be overlooked if relative spin populations were used as a measure of preparation fidelity [42,46–48]. Using this metric, $T(\rho = \sigma_{22}, \sigma_{22}) = 0$ indicates that the prepared state is indistinguishable from the target state (unity initialization fidelity). Conversely, $T(\rho, \sigma_{22}) = 1$ indicates that the prepared state is orthogonal to the target state, and is therefore completely distinguishable.

For both the single and bimodal cavity configurations, we choose the Y-polarized mode to be resonant with the $|2\rangle \rightarrow |4\rangle$ transition [i.e., $\nu_Y = \omega_0 + (\Delta_B^h - \Delta_B^e)/2$]. However, when coupled to a bimodal cavity, we leave the X-polarized cavity mode detuned from the corresponding transitions such that $\nu_X = \omega_0$ as this has been shown to maximize the initialization fidelity with this cavity configuration [42].

To allow a direct comparison between the two cavity configurations, we assume that spin initialization is achieved by directly driving the QD transitions. This differs from previous work studying spin initialization with bimodal cavities, which used cavity driving rather than direct QD driving to initialize the spin state [42]. However, both schemes lead to qualitatively the same behavior and, importantly, considering only one driving configuration, allows a fair and consistent comparison between the individual cavity setups [49].

A. Steady-state limit

Using the model in Sec. II, we begin by studying initialization in the steady-state limit with a continuous wave (CW) driving term [i.e., $\Omega_X(t) = \Omega_X \; \forall \, t$]. While this limit does not accurately reflect experimental procedures for initializing spin states, the steady state still provides an insight into the behavior of the system and limits the available parameter space. Figures 2(b) and 2(c) show the calculated trace distance between the prepared steady state and target state with a fixed driving strength as a function of g/κ for a range of cavity linewidths.

The results presented in Fig. 2 show that in the steady-state limit, the inclusion of cavity effects reduces the initialization fidelity. For small g, this is a result of the cavity modifying the lifetime of the trion states, and thus the ratio Ω/γ. As the cavity coupling strength is increased, the fixed driving strength is no longer optimized to achieve the smallest trace distance. We therefore find that for each set of cavity parameters, the Rabi frequency needs to be optimized to minimize the trace distance. As the cavity-coupled system enters the strong-coupling regime ($g \gg \kappa, \gamma$), the QD states hybridize with the cavity modes, fundamentally changing the system eigenstructure, which leads to a maximally mixed ground state, where $T(\rho, \sigma_{11}) = T(\rho, \sigma_{22}) = 0.5$. For a bimodal cavity setup, we find that the steady state evolves to return $0.1 \leqslant T(\rho, \sigma_{22}) \leqslant 0.5$ depending on the cavity linewidth.

In the limit of the narrowest cavity linewidths, we expect both cavity configurations to display similar behavior. At these linewidths, only the $|4\rangle \rightarrow |2\rangle$ transition experiences a significant Purcell enhancement in either cavity configuration, with all other optical transitions sufficiently detuned from the cavity mode to experience little to no enhancement. This expectation is borne out in Fig. 2 with $\kappa/2\pi = 1$ GHz. At this cavity linewidth, both cavity configurations return similar trace distances, with small differences resulting from some nonzero enhancement of the X-polarized transitions when coupled to a bimodal cavity.

With large coupling strengths, we find the bimodal cavity outperforms the single-mode cavity, returning smaller trace distances for $1 < \kappa/2\pi < 100$ GHz. At intermediate cavity linewidths, the Purcell enhancement of the $|3\rangle \rightarrow |2\rangle$ transition is greater than that of the $|3\rangle \rightarrow |1\rangle$ transition. Thus any population in the $|3\rangle$ state excited through off-resonant driving will preferentially decay back to the desired $|2\rangle$ state, providing additional protection to the prepared state. While the Purcell enhancement of the $|4\rangle \rightarrow |1\rangle$ transition does hinder the initialization process, this effect is less significant in the limit of infinite driving time. Increasing the cavity linewidth begins to equalize the enhancement of the transitions away from the $|3\rangle$ state, and hence the system tends towards the maximally mixed ground state with $T(\rho, \sigma_{22}) = 0.5$ as in the single-mode case.

B. Finite pulse duration

While the limit of infinite driving time provides some insight into the system behaviors, it does not accurately reflect the experimental realization of optical spin initialization. Any experimentally relevant protocol requires the initialization process to occur in a finite time, and is thus achieved with finite optical pulses rather than CW drive. Maximizing the spin initialization fidelity in this limit of finite driving time requires maximizing the efficiency and speed with which the spin population is transferred from the $|1\rangle$ state to the $|2\rangle$ state. Thus we now consider the impact of cavity coupling on the initialization of the spin system when driven by a finite optical pulse with either a square or Gaussian envelope.

As pulsed optical driving is a more accurate representation of the experimental realization of optical spin initialization, we now opt to calculate $T(\rho, \sigma_{22})$ as a function of more experimentally accessible parameters, namely, the Purcell factor and cavity linewidth. The combination of the light-matter coupling strength and cavity linewidth leads to an enhanced emission rate from the relevant optical transition quantified through the Purcell enhancement $F_P(\lambda) = 4|g_\lambda|^2/\kappa_\lambda\gamma_\lambda$ when on resonance [31]. We shall restrict the cavity linewidth and Purcell factor to $1 \leqslant \kappa/2\pi \leqslant 110$ GHz and $1 \leqslant F_P \leqslant 40$, respectively. This maintains the Purcell enhancement in a regime that has been experimentally demonstrated [31], and limits the cavity quality factors to experimentally achievable values (of the order of 10^3–10^5 for wavelengths in the NIR and telecommunications bands).

1. *Square pulse*

We first examine initialization with a finite square pulse with $\Omega_X(t) = \Omega[H(t - t_0 + \Delta\tau_X/2) - H(t - t_0 - \Delta\tau_X/2)]$, where $H(x)$ is the Heaviside function, t_0 is the center of the pulse, $\Delta\tau_X$ is the pulse duration, and Ω is the Rabi frequency of the pulse. For a given set of cavity parameter combinations, we vary the Rabi frequency of the pulse in the range $0 \leqslant \Omega_X \leqslant 10\gamma$ to find the minimum trace distance for each pulse duration $\Delta\tau_X$, leaving adequate time after the pulse for the trion populations to fully decay. Figures 3(a)–3(c) show the resulting minimized trace distance as a function of the pulse duration for single-mode and bimodal cavity structures for different cavity parameters. The effects of pure dephasing are discussed in the Appendix and are shown to have similarly negligible effects for either cavity configuration when driving with a square pulse.

Irrespective of cavity configuration, we find a general trend of decreasing trace distance with increasing pulse duration. Longer pulse durations both increase the fraction of the $|1\rangle$ state population transferred to the excited state, and, when the pulse duration is longer than the excited state lifetime, enable the reexcitation of any nonzero $|1\rangle$ population resulting from the decay of the trion states via the $|4\rangle \rightarrow |1\rangle$ and $|3\rangle \rightarrow |1\rangle$ transitions. Furthermore, increasing the duration of the driving pulse decreases its bandwidth, which, in turn,

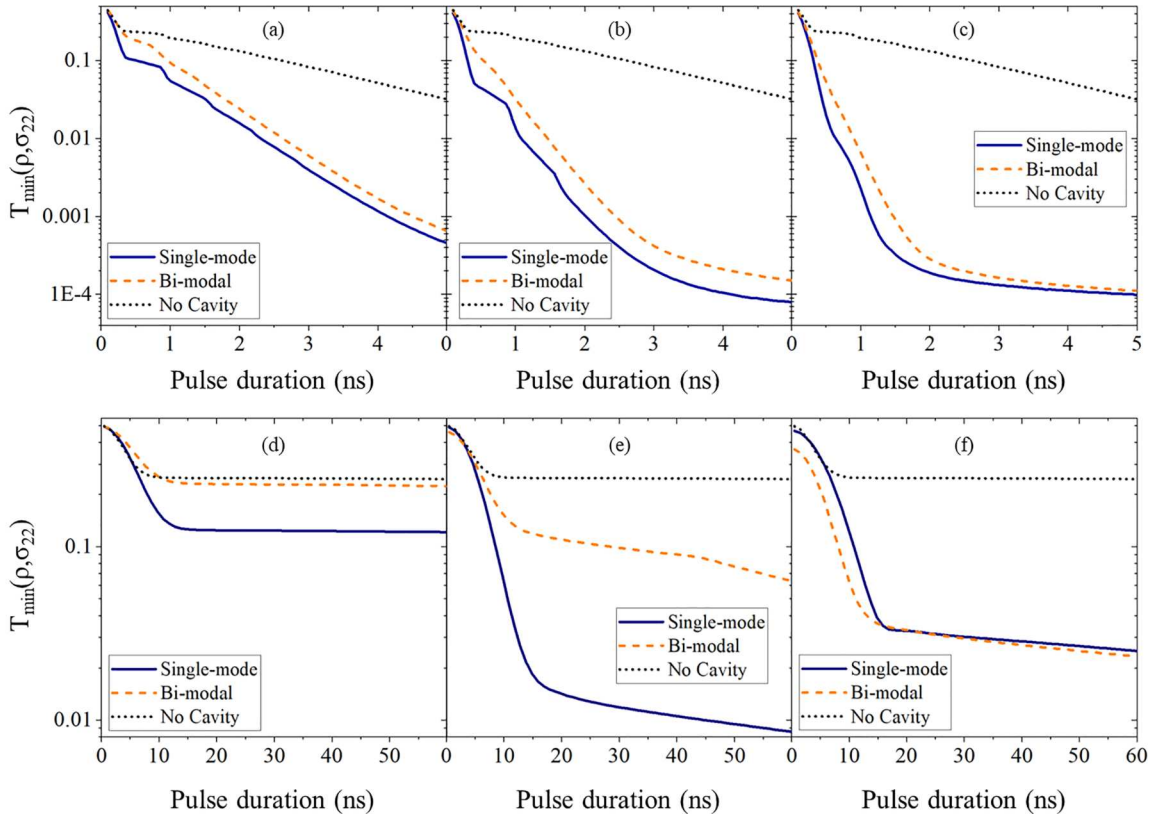

FIG. 3. The calculated trace distances between the final state of the four-level system and the target state as a function of the duration of the driving pulse when driving with a top-hat (top) or Gaussian (bottom) pulse. The trace distances are presented for the single-mode (blue solid) and bimodal (orange dash) cavity configurations, as well as without a cavity (black dot), and are minimized with respect to the driving strength (peak Rabi frequency and pulse area for square and Gaussian pulses, respectively). The cavity parameters used are (a) $\kappa/2\pi = 110$ GHz, $F_P = 2$, (b) $\kappa/2\pi = 47$ GHz, $F_P = 5$, (c) $\kappa/2\pi = 21$ GHz, $F_P = 10$, (d) $\kappa/2\pi = 110$ GHz, $F_P = 2$, (e) $\kappa/2\pi = 33$ GHz, $F_P = 40$, and (f) $\kappa/2\pi = 6$ GHz, $F_P = 40$. Other parameters: $B = 5$ T, $g_{e(h)} = 0.5(0.3)$, $\gamma^{-1} = 1$ ns, $\nu_X = \omega_0$, and $\nu_Y = \omega_0 + (\Delta_B^h - \Delta_B^e)/2$.

reduces the strength of the off-resonant driving of the $|2\rangle \rightarrow |3\rangle$ transition that moves the system away from the target state.

When coupled to a single-mode cavity and driving with a square pulse, we find the Purcell enhancement of the resonant Y-polarized transition is the most important factor in achieving a high initialization fidelity. For the majority of the studied cavity parameter combinations, the effect of the cavity linewidth only becomes significant at longer pulse durations, depending on the Purcell factor. We find that neither the largest Purcell factor nor the narrowest cavity linewidth that is studied necessarily produces the best fidelity in the limit of finite pulse duration. Instead of the studied cavity parameter combinations, an intermediate linewidth of $\kappa/2\pi = 20$ GHz and Purcell factor of $F_P = 10$ produced the smallest trace distance over the largest range of pulse durations. Maximizing the initialization fidelity requires balancing the rates at which the system is driven to and from the target state. An intermediate cavity linewidth is required to avoid the cyclical reexcitation of the $|4\rangle$ state that would occur in the strong-coupling regime, and act to increase $T(\varrho, \sigma_{22})$. However, to limit the rate at which the system is driven away from the target $|2\rangle$ state owing to the increased spectral bandwidth of the finite pulse, the Purcell factor must also be limited to minimize the decay rate of the unwanted $|3\rangle \rightarrow |1\rangle$ transition.

Similar results are found when the QD is coupled to a bimodal cavity. Again, the Purcell enhancement of the resonant Y-polarized transition appears to be the dominant factor in determining the trace distance as a function of pulse duration. However, relative to initialization with a single-mode cavity, the calculated trace distances are larger and require a longer pulse duration to achieve. In this configuration, we find that a Purcell factor of $F_P = 40$ produces the largest trace distances for the majority of the studied cavity linewidths. For the considered cavity parameters, we find that $F_P = 10$ and $\kappa/2\pi = 1$ GHz produce the best initialization fidelity with pulse durations less than $\approx$0.5 ns, while $F_P = 10$ and $\kappa/2\pi = 20$ GHz produce the best initialization fidelity for pulse durations greater than $\approx$0.5 ns.

Plateaus and regions of decreased gradient in the trace distance can also be seen in Figs. 3(a)–3(c). These plateaus are artifacts of the limiting range over which the Rabi frequency is swept for each data point. Driving the system with increasing Rabi frequency naturally results in Rabi oscillations in the system populations. The edge of each plateau occurs when the pulse duration is long enough to encompass the next oscillation with a lower local minimum than the previous one. These plateaus are not seen at longer pulse durations as the global minimum in the trace distance as a function of Rabi frequency usually occurs after two or three oscillations.

2. Gaussian pulse

We now move on to study initialization with a Gaussian optical pulse. We define the Gaussian pulse with polarization $\lambda = X, Y$ centered around t_0 as

$$\Omega_\lambda(t) = \frac{\Theta_\lambda}{\sqrt{2\pi w_\lambda^2}} \exp\left\{-\frac{(t-t_0)^2}{2w_\lambda^2}\right\}, \tag{6}$$

where $\Theta_\lambda = \int_{-\infty}^{\infty} dt\, \Omega_\lambda(t)$ is the pulse area defined such that a pulse with $\Theta_\lambda = \pi$ would invert the population of a two-level system, and w_λ is the Gaussian width of the pulse related to the intensity full width at half maximum ($\Delta\tau_\lambda$) by

$$w_\lambda = \frac{\Delta\tau_\lambda}{2\sqrt{\ln 2}}. \tag{7}$$

Following the procedure for the finite square pulse, we plot the trace distance, minimized with respect to the pulse area in the range $0.01\pi \leqslant \Theta_X \leqslant 5\pi$, as a function of $\Delta\tau_X$. Figures 3(d)–3(f) show the results for Gaussian pulsed excitation.

Just as with the square optical pulse, we find that the trace distance decreases with increasing pulse duration. Spin initialization with Gaussian pulses occurs on much shorter timescales than when using square pulses, with the trace distance being optimized in tens of picoseconds rather than a few nanoseconds. Additionally, the trace distances achieved with a Gaussian pulse are smaller than those achieved with the shortest square pulses that are studied (<1 ns), which are unlikely to be experimentally accessible. However, the smallest achieved trace distances driving with a Gaussian pulse are orders of magnitude larger than those found when driving with a longer square pulse (>1 ns). Below $\Delta\tau_X \lessapprox 15$ ps, this is a consequence of the bandwidth of the driving pulse resulting in a significant spectral overlap between the driving field and the off-resonant $|2\rangle \rightarrow |3\rangle$ transition, which, in turn, increases the driving of the system away from the desired state. However, beyond $\Delta\tau_X \approx 15$ ps, this overlap is minimized and thus the trace distance is governed by reexcitation of population that initially decayed into the unwanted ground state ($|1\rangle$). This, in turn, is limited by the ratio of the decay rate of the trion states into the $|1\rangle$ state and the pulse duration. Furthermore, attaining these trace distances when driving with a Gaussian pulse requires the largest Purcell enhancement for all but the narrowest cavity linewidths due to the pulse duration being much shorter than the trion lifetimes, which can prove challenging to realize experimentally.

We again find that coupling the QD to a bimodal cavity significantly increases the calculated trace distances after the initialization procedure. In fact, for some of the cavity parameters studied for the bimodal case, the produced trace distances are comparable to initialization with a Gaussian pulse in the absence of any cavity effects. However, the Appendix shows that when driving with a Gaussian pulse, spin initialization with a bimodal cavity configuration is the most robust against pure dephasing.

IV. SPIN READOUT

In addition to high-fidelity spin initialization, it is crucial that the cavity structures are also conducive to high-fidelity readout. We therefore study optical spin readout for both single mode and bimodal cavities using the method first proposed in [23] and demonstrated experimentally in [24]. This readout method uses the spin-dependent transmissivity or reflectivity of a cavity mode resonantly coupled to a transition of the QD to determine its spin state. In contrast to Ref. [23], we choose the cavity configuration to mirror the setup used for high-fidelity spin initialization, where the cavity mode is coupled to the Y-polarized transitions. The $|2\rangle \rightarrow |4\rangle$ transition is then weakly probed by a resonant drive via the Y-polarized cavity mode present in either cavity configuration. If the emitter occupies the $|1\rangle$ state, the photons are transmitted, while if the QD resides in the $|2\rangle$ state, the photons are reflected [see Fig. 4(a)]. By comparing the ratio of photons transmitted versus incident with a threshold value [23], the state ($|1\rangle$ or $|2\rangle$) occupied by the QD can be determined.

The readout protocol is initialized by weakly probing the Y-polarized cavity mode over some time interval $[0, \tau]$, where τ is much longer than the lifetime of the system. Over this time interval, we set a threshold photon number k, where, if the number of collected transmitted photons is less than k, then the qubit state is $|2\rangle$, otherwise it is $|1\rangle$. The maximum probability of a successful readout occurring is then given by $\mathcal{R} = \max_k[q_1 p_1(k) + q_2 p_2(k)]$, where q_i is the probability of finding the qubit in state i, and p_i is the probability of getting a correct result using threshold photon number k. As shown by Ref. [23], for detectors with a dead time shorter than the interval between detection events, and in the weak driving limit, the probabilities $p_i(k)$ can be described by Poissonian statistics. This allows the readout fidelity ($\mathcal{R}$) to be written as [23]

$$\mathcal{R}(\tau) = \frac{1}{2} - \frac{1}{2}\sum_{k=0}^{M}\frac{1}{k!}\left\{[N_1(\tau)]^k e^{-N_1(\tau)} - [N_2(\tau)]^k e^{-N_2(\tau)}\right\}, \tag{8}$$

where M is the optimal threshold value [23],

$$M = \left\lfloor \frac{N_2(\tau) - N_1(\tau)}{\ln[N_2(\tau)] - \ln[N_1(\tau)]} \right\rfloor, \tag{9}$$

with $\lfloor x \rfloor$ indicating the largest integer smaller than x, and N_i is the number of photons emitted from the cavity mode when the QD starts in the ground state $|i = 1, 2\rangle$. The number of photons emitted can be found by integrating the output flux of the cavity over the duration of the optical readout pulse,

$$N_{i,\lambda}(\tau) = \eta\kappa_\lambda \int_0^\tau \left|\mathrm{Tr}[a_\lambda^\dagger a_\lambda \rho_i(t)]\right| dt. \tag{10}$$

Here, τ is the duration of the readout pulse, η is the photon collection efficiency, and $\rho_i(t)$ are the density matrices of the system at time t when the QD is initialized in the ground state $|i = 1, 2\rangle$. We also continue to assume both modes of the bimodal cavity have identical linewidths such that $\kappa_{\lambda=X,Y} = \kappa$. This readout method has been demonstrated to work experimentally, producing $\mathcal{R} = 0.61$ with a cavity linewidth $\kappa/2\pi = 67$ GHz, an enhancement factor $F_P = 62$, a collection efficiency $\eta = 4.1 \times 10^{-3}$, and 75 ns pulse duration [24].

Considering a square pulse with a duration of 35 ns [50] and time-dependent cavity driving strength

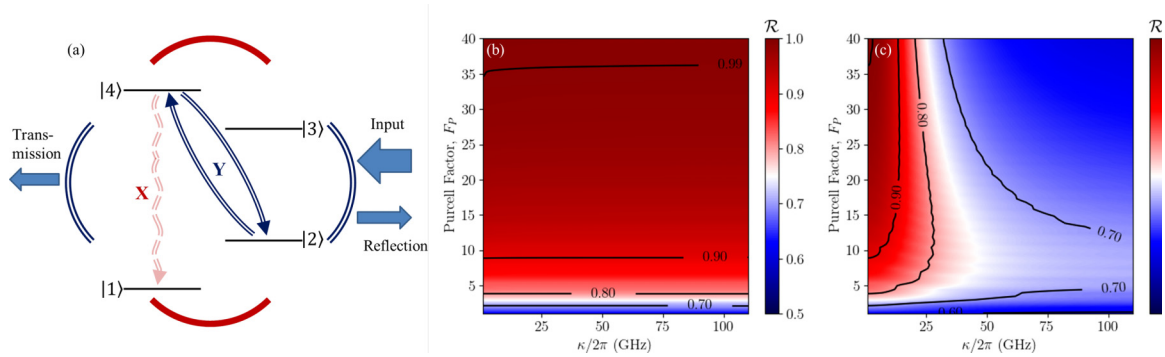

FIG. 4. (a) A diagram of the spin-readout process. The Y-polarized cavity mode is probed with a square laser pulse and the QD-state-dependent reflectivity/transmissivity is measured. By comparing the collected photon number with a threshold value, the spin state of the system may be determined. (b), (c) The calculated readout fidelities (R) for a single-mode cavity and a bimodal cavity, respectively, when driving the Y-polarized cavity mode with a 35 ns square pulse. Parameters: $B = 5$ T, $g_{e(h)} = 0.5(0.3)$, $\gamma^{-1} = 1$ ns, $\epsilon_Y = \sqrt{(0.01 \times 2g_Y^2)}$, $\eta = 1$, $\nu_X = \omega_0$, and $\nu_Y = \omega_0 + (\Delta_B^h - \Delta_B^e)/2$.

$\epsilon_Y(t) = \sqrt{(0.01 \times 2g_Y^2)}$ for $t \in [0, 35\ \text{ns}]$ to remain in the weak-excitation regime [23], and assuming $\eta = 1$, we calculate the spin-readout fidelity for a range of cavity parameters. The weak-excitation regime is used in the readout stage to limit readout-induced errors resulting from the readout pulse influencing the state of the system. Figures 4(b) and 4(c) show these results for a single-mode and bimodal cavity, respectively. In the case of the single-mode cavity, we find the readout fidelity is primarily dependent on the Purcell enhancement of the Y-polarized transitions, and varies little with respect to κ_Y. This is because the Purcell enhancement increases the strength of the quasicycling transition required to produce a detectable readout signal, while the cavity linewidth has little impact on the Purcell enhancement of the resonant transition being probed. Figure 4(b) shows that $F_P = 7$ gives $\mathcal{R} \approx 90\%$.

In contrast, the bimodal readout fidelity is sensitive to both the cavity linewidth and Purcell enhancement of the optical transitions. The highest readout fidelities with this cavity configuration are produced with narrow cavity linewidths and large Purcell factors, which prevent undesirable transitions from being Purcell enhanced. This increases the cyclicity of the Λ-systems, which naturally increases the strength of the quasicycling transition probed during the readout procedure. To achieve $\mathcal{R} > 90\%$ with a bimodal cavity requires $\kappa/2\pi \leqslant 13$ GHz and $F_P \geqslant 9$. Note that under these driving conditions, when the cavity parameters are optimized for either cavity configuration, we find that a collection efficiency of $\eta \geqslant 48\%$ gives $\mathcal{R} \geqslant 99\%$. Such collection efficiencies have already been demonstrated in an open-access microcavity system [33]; for planar PhC or nanobeam structures, very high efficiencies could be achieved by direct fiber coupling [51,52]. The effects of pure dephasing on the readout fidelity are shown in the Appendix. We find that while increasing the pure dephasing rate increases the required Purcell factors for both cavity configurations, the single-mode cavity is more robust against these processes in the readout stage.

V. CONCLUSION

By performing full cavity QED calculations, we have investigated optical spin initialization and readout for a QD interacting with either single-mode or bimodal optical cavities. Interestingly, we find that for both initialization and readout, a single-mode optical cavity outperforms the bimodal cavity over the full parameter regime that is studied, regardless of the pulse envelope that is used. This is a consequence of the bimodal cavity Purcell enhancing undesirable transitions, therefore suppressing desired spin-flip processes. While these unwanted transitions can be suppressed for spin preparation, we find that they restrict the parameter regimes for which high-fidelity optical spin readout can be achieved with bimodal cavities. Furthermore, this range of optimal readout cavity parameters (large F_P) does not overlap with the small range of cavity parameters required for optimized spin initialization in a bimodal cavity (small F_P).

In contrast, we have shown that a near unity readout fidelity is possible with a single-mode cavity across the vast majority of the studied cavity parameters. In the single-mode configuration with experimentally achievable [53–55] cavity parameters ($\kappa/2\pi = 20$ GHz, $F_P = 10$), we find an initialization trace distance $T(\rho, \sigma_{22}) = 1.3 \times 10^{-4}$ is achievable with a 3 ns square optical pulse, while a readout success probability of $\mathcal{R} > 0.90$ is possible with a 35 ns optical pulse. Increasing the Purcell factor to $F_P = 35$ increases the readout success rate to $\mathcal{R} = 0.99$ while maintaining an initialization trace distance of the order of 10^{-4}. For a bimodal system using the same parameters, a comparable initialization trace distance of $T(\rho, \sigma_{22}) = 2.2 \times 10^{-4}$ is achievable. However, the corresponding readout success rate is reduced to $\mathcal{R} \approx 0.88$. In the parameter regimes studied here, no single set of bimodal cavity parameters simultaneously allows for high-fidelity spin initialization and readout with finite optical pulses.

These results suggest that to realize a high-fidelity spin-photon interface, a single linearly polarized cavity mode providing a modest (∼20) Purcell enhancement is the optimal configuration. In addition, further calculations presented in the Appendix demonstrate that this parameter regime is also robust against significant levels of pure dephasing, illustrating the potential to achieve high-performance spin-photon interfaces in real physical systems. For inherently bimodal cavities such as micropillars or point defects in PhCs, our analysis suggests that there would be significant benefit in modifying designs to induce a mode splitting much larger than the cavity

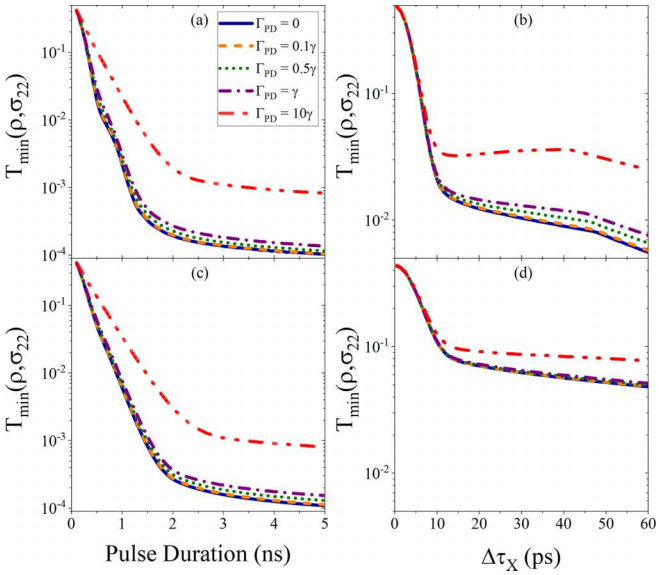

FIG. 5. The calculated trace distance between the state prepared by the initialization process and the target state minimizing with respect to the driving strength when driving with a (a), (c) square pulse or (b), (d) Gaussian pulse, and coupled to a (a), (b) single-mode or (c), (d) bimodal cavity for different pure dephasing rates indicated in the legend in (a) using the cavity parameters that minimize the trace distance in the absence of pure dephasing processes. Parameters used: $\gamma^{-1} = 1$ ns, (a), (c) $\kappa/2\pi = 20$ GHz, $F_P = 10$, (b) $\kappa/2\pi = 40$ GHz, $F_P = 40$, and (d) $\kappa/2\pi = 20$ GHz, $F_P = 40$.

linewidth (e.g., elliptical micropillars [34]). We believe that these insights and methods will contribute to the development of high-fidelity spin-photon interfaces that meet the stringent requirements of future optical quantum technologies.

ACKNOWLEDGMENTS

The authors would like to acknowledge the funding support of the University of Sheffield, and the Engineering and Physical Sciences Research Council (EPSRC) (UK) Grants No. EP/N031776/1 and No. EP/V026496/1. A.J.B. acknowledges support from the EPSRC (UK) fellowship, Grant No. EP/W027909/1.

APPENDIX: PURE DEPHASING

Thus far, we have assumed that the trion states are lifetime limited. However, in physical systems, elastic processes will occur that preserve the spin populations, but reduce their coherence. We therefore also study the effect of pure dephasing of the trion states on the spin initialization and readout processes when driving with a finite duration pulse. We account for pure dephasing through the addition of further Lindblad terms,

$$\sum_{j=3,4} \frac{\Gamma}{2} \mathcal{L}_{\sigma_{jj}}[\rho(t)], \tag{A1}$$

in the master equation. Here, Γ is the pure dephasing rate, and $\mathcal{L}_O[\rho] = 2O\rho O^\dagger - \{O^\dagger O, \rho\}$ is the Lindblad superoperator.

1. Spin initialization

To study the influence of pure dephasing in the optical initialization process, we follow the same procedure presented in Sec. III, sweeping the duration of the given optical pulse and minimizing the trace distance with respect to the Rabi frequency or pulse area. However, we now only consider the combination of cavity parameters that produced the smallest trace distance in the absence of pure dephasing for a given pulse envelope, and instead plot the calculated trace distances for a number of pure dephasing rates.

Figure 5 shows that when $\Gamma \leqslant \gamma$, pure dephasing has a minimal impact on the calculated trace distances after the initialization process for any combination of driving pulse envelope and cavity configuration. For $\Gamma \gg \gamma$, Fig. 5 shows that pure dephasing significantly increases the calculated trace distances. For all studied combinations, the divergence between the traces distances calculated neglecting and including pure dephasing increases with increasing pulse duration. However, while producing the largest minimized trace distance, optical spin initialization with the combination of a bimodal cavity and Gaussian pulse drive appears the least susceptible to the influence of pure dephasing. The Purcell enhancement of all four optical transitions, combined with the fast optical driving, work to reduce the relative impact of pure dephasing mechanisms by minimizing the time the system spends in the excited states. Nevertheless, we note that for all configurations, small trace distances are achievable even in the presence of significant pure dephasing.

2. Spin readout

To study the impact of pure dephasing on the spin-readout process, we calculate the readout success probability for two pure dephasing rates, $\Gamma = \gamma$ and $\Gamma = 10\gamma$. Figure 6 shows

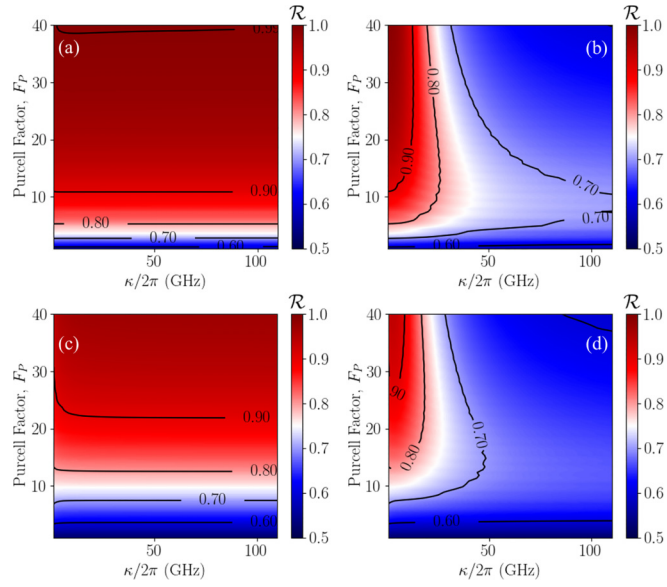

FIG. 6. The calculated spin-readout success probabilities when coupled to a (a), (c) single-mode or (b), (d) bimodal cavity when the 4LS experiences pure dephasing with rates (a), (b) $\Gamma = \gamma$ and (c), (d) $\Gamma = 10\gamma$. Parameters used: $B = 5$ T, $g_{e(h)} = 0.5(0.3)$, $\gamma^{-1} = 1$ ns, $\epsilon_Y = \sqrt{(0.01 \times 2g_Y^2)}$, $\eta = 1$, $\nu_X = \omega_0$, and $\nu_Y = \omega_0 + (\Delta_B^h - \Delta_B^e)/2$.

the results when coupled to a single-mode or bimodal cavity. When coupled to a single-mode cavity, Figs. 6(a) and 6(c) show that the readout process is impacted by pure dephasing. While, at $\Gamma = \gamma$, $\mathcal{R} > 0.99$ is still just achievable in the studied parameter regimes, by increasing the pure dephasing rate to $\Gamma = 10\gamma$, this is no longer achievable although there remains a significant region where $\mathcal{R} > 0.9$. When coupled to a bimodal cavity, increasing the pure dephasing rate from $\Gamma = \gamma$ to $\Gamma = 10\gamma$ roughly halves the parameter regime where $\mathcal{R} >= 0.9$ is achievable.

[1] M. Kroutvar, Y. Ducommun, D. Heiss, M. Bichler, D. Schuh, G. Abstreiter, and J. J. Finley, Optically programmable electron spin memory using semiconductor quantum dots, Nature (London) **432**, 81 (2004).

[2] G. Gillard, I. M. Griffiths, G. Ragunathan, A. Ulhaq, C. McEwan, E. Clarke, and E. A. Chekhovich, Fundamental limits of electron and nuclear spin qubit lifetimes in an isolated self-assembled quantum dot, npj Quantum Inf. **7**, 43 (2021).

[3] D. Press, K. De Greve, P. L. McMahon, T. D. Ladd, B. Friess, C. Schneider, M. Kamp, S. Höfling, A. Forchel, and Y. Yamamoto, Ultrafast optical spin echo in a single quantum dot, Nat. Photon. **4**, 367 (2010).

[4] A. Bechtold, D. Rauch, F. Li, T. Simmet, P.-L. Ardelt, A. Regler, K. Müller, N. A. Sinitsyn, and J. J. Finley, Three-stage decoherence dynamics of an electron spin qubit in an optically active quantum dot, Nat. Phys. **11**, 1005 (2015).

[5] H. J. Kimble, The quantum internet, Nature (London) **453**, 1023 (2008).

[6] N. H. Lindner and T. Rudolph, Proposal for pulsed on-demand sources of photonic cluster state strings, Phys. Rev. Lett. **103**, 113602 (2009).

[7] E. V. Denning, J. Iles-Smith, D. P. S. McCutcheon, and J. Mork, Protocol for generating multiphoton entangled states from quantum dots in the presence of nuclear spin fluctuations, Phys. Rev. A **96**, 062329 (2017).

[8] D. Scerri, R. N. E. Malein, B. D. Gerardot, and E. M. Gauger, Frequency-encoded linear cluster states with coherent raman photons, Phys. Rev. A **98**, 022318 (2018).

[9] I. Schwartz, D. Cogan, E. R. Schmidgall, Y. Don, L. Gantz, O. Kenneth, N. H. Lindner, and D. Gershoni, Deterministic generation of a cluster state of entangled photons, Science **354**, 434 (2016).

[10] D. Cogan, Z.-E. Su, O. Kenneth, and D. Gershoni, Deterministic generation of indistinguishable photons in a cluster state, Nat. Photon. **17**, 324 (2023).

[11] N. Coste, D. A. Fioretto, N. Belabas, S. C. Wein, P. Hilaire, R. Frantzeskakis, M. Gundin, B. Goes, N. Somaschi, M. Morassi, A. Lemaître, I. Sagnes, A. Harouri, S. E. Economou, A. Auffeves, O. Krebs, L. Lanco, and P. Senellart, High-rate entanglement between a semiconductor spin and indistinguishable photons, Nat. Photon. **17**, 582 (2023).

[12] M. H. Appel, A. Tiranov, S. Pabst, M. L. Chan, C. Starup, Y. Wang, L. Midolo, K. Tiurev, S. Scholz, A. D. Wieck, A. Ludwig, A. S. Sørensen, and P. Lodahl, Entangling a hole spin with a time-bin photon: A waveguide approach for quantum dot sources of multiphoton entanglement, Phys. Rev. Lett. **128**, 233602 (2022).

[13] Y. Meng, C. F. Faurby, M. L. Chan, P. I. Sund, Z. Liu, Y. Wang, N. Bart, A. D. Wieck, A. Ludwig, L. Midolo, A. S. Sørensen, S. Paesani, and P. Lodahl, Photonic fusion of entangled resource states from a quantum emitter, arXiv:2312.09070.

[14] S. Sun, H. Kim, G. S. Solomon, and E. Waks, A quantum phase switch between a single solid-state spin and a photon, Nat. Nanotechnol. **11**, 539 (2016).

[15] S. Sun, H. Kim, Z. Luo, G. S. Solomon, and E. Waks, A single-photon switch and transistor enabled by a solid-state quantum memory, Science **361**, 57 (2018).

[16] J. Borregaard, H. Pichler, T. Schröder, M. D. Lukin, P. Lodahl, and A. S. Sørensen, One-way quantum repeater based on near-deterministic photon-emitter interfaces, Phys. Rev. X **10**, 021071 (2020).

[17] W. J. Munro, A. M. Stephens, S. J. Devitt, K. A. Harrison, and K. Nemoto, Quantum communication without the necessity of quantum memories, Nat. Photon. **6**, 777 (2012).

[18] M. Atatüre, J. Dreiser, A. Badolato, A. Högele, K. Karrai, and A. Imamoglu, Quantum-dot spin-state preparation with near-unity fidelity, Science **312**, 551 (2006).

[19] D. Kim, S. E. Economou, Ş. C. Bădescu, M. Scheibner, A. S. Bracker, M. Bashkansky, T. L. Reinecke, and D. Gammon, Optical spin initialization and nondestructive measurement in a quantum dot molecule, Phys. Rev. Lett. **101**, 236804 (2008).

[20] A cycling transition is one which returns the system to its original spin state in a cyclical fashion.

[21] A. Delteil, W. B. Gao, P. Fallahi, J. Miguel-Sanchez, and A. Imamoğlu, Observation of quantum jumps of a single quantum dot spin using submicrosecond single-shot optical readout, Phys. Rev. Lett. **112**, 116802 (2014).

[22] N. O. Antoniadis, M. R. Hogg, W. F. Stehl, A. Javadi, N. Tomm, R. Schott, S. R. Valentin, A. D. Wieck, A. Ludwig, and R. J. Warburton, Cavity-enhanced single-shot readout of a quantum dot spin within 3 nanoseconds, Nat. Commun. **14**, 3977 (2023).

[23] S. Sun and E. Waks, Single-shot optical readout of a quantum bit using cavity quantum electrodynamics, Phys. Rev. A **94**, 012307 (2016).

[24] S. Sun, H. Kim, G. S. Solomon, and E. Waks, Cavity-enhanced optical readout of a single solid-state spin, Phys. Rev. Appl. **9**, 054013 (2018).

[25] M. H. Appel, A. Tiranov, A. Javadi, M. C. Löbl, Y. Wang, S. Scholz, A. D. Wieck, A. Ludwig, R. J. Warburton, and P. Lodahl, Coherent spin-photon interface with waveguide induced cycling transitions, Phys. Rev. Lett. **126**, 013602 (2021).

[26] C. Emary, X. Xu, D. G. Steel, S. Saikin, and L. J. Sham, Fast initialization of the spin state of an electron in a quantum dot in the voigt configuration, Phys. Rev. Lett. **98**, 047401 (2007).

[27] M. Arcari, I. Söllner, A. Javadi, S. Lindskov Hansen, S. Mahmoodian, J. Liu, H. Thyrrestrup, E. H. Lee, J. D. Song, S. Stobbe, and P. Lodahl, Near-unity coupling efficiency of a quantum emitter to a photonic crystal waveguide, Phys. Rev. Lett. **113**, 093603 (2014).

[28] A. Reinhard, T. Volz, M. Winger, A. Badolato, K. J. Hennessy, E. L. Hu, and A. Imamoğlu, Strongly correlated photons on a chip, Nat. Photon. **6**, 93 (2012).

[29] R. Ohta, Y. Ota, M. Nomura, N. Kumagai, S. Ishida, S. Iwamoto, and Y. Arakawa, Strong coupling between a photonic crystal nanobeam cavity and a single quantum dot, Appl. Phys. Lett. **98**, 173104 (2011).

[30] J. P. Reithmaier, G. Sęk, A. Löffler, C. Hofmann, S. Kuhn, S. Reitzenstein, L. V. Keldysh, V. D. Kulakovskii, T. L. Reinecke, and A. Forchel, Strong coupling in a single quantum dot-semiconductor microcavity system, Nature (London) **432**, 197 (2004).

[31] F. Liu, A. J. Brash, J. O'Hara, L. M. P. P. Martins, C. L. Phillips, R. J. Coles, B. Royall, E. Clarke, C. Bentham, N. Prtljaga, I. E. Itskevich, L. R. Wilson, M. S. Skolnick, and A. M. Fox, High Purcell factor generation of indistinguishable on-chip single photons, Nat. Nanotechnol. **13**, 835 (2018).

[32] K. Rivoire, S. Buckley, and J. Vučković, Multiply resonant high quality photonic crystal nanocavities, Appl. Phys. Lett. **99**, 013114 (2011).

[33] N. Tomm, A. Javadi, N. O. Antoniadis, D. Najer, M. C. Löbl, A. R. Korsch, R. Schott, S. R. Valentin, A. D. Wieck, A. Ludwig, and R. J. Warburton, A bright and fast source of coherent single photons, Nat. Nanotechnol. **16**, 399 (2021).

[34] H. Wang, Y.-M. He, T.-H. Chung, H. Hu, Y. Yu, S. Chen, X. Ding, M.-C. Chen, J. Qin, X. Yang, R.-Z. Liu, Z.-C. Duan, J.-P. Li, S. Gerhardt, K. Winkler, J. Jurkat, L.-J. Wang, N. Gregersen, Y.-H. Huo, Q. Dai, Towards optimal single-photon sources from polarized microcavities, Nat. Photon. **13**, 770 (2019).

[35] R. J. Coles, N. Prtljaga, B. Royall, I. J. Luxmoore, A. M. Fox, and M. S. Skolnick, Waveguide-coupled photonic crystal cavity for quantum dot spin readout, Opt. Express **22**, 2376 (2014).

[36] U. M. Gür, M. Mattes, S. Arslanagić, and N. Gregersen, Elliptical micropillar cavity design for highly efficient polarized emission of single photons, Appl. Phys. Lett. **118**, 061101 (2021).

[37] B. Gayral, J. M. Gérard, B. Legrand, E. Costard, and V. Thierry-Mieg, Optical study of GaAs/AlAs pillar microcavities with elliptical cross section, Appl. Phys. Lett. **72**, 1421 (1998).

[38] S. Reitzenstein, C. Hofmann, A. Gorbunov, M. Strauß, S. H. Kwon, C. Schneider, A. Löffler, S. Höfling, M. Kamp, and A. Forchel, Al As/Ga As micropillar cavities with quality factors exceeding 150.000, Appl. Phys. Lett. **90**, 251109 (2007).

[39] I. J. Luxmoore, E. D. Ahmadi, B. J. Luxmoore, N. A. Wasley, A. I. Tartakovskii, M. Hugues, M. S. Skolnick, and A. M. Fox, Restoring mode degeneracy in H1 photonic crystal cavities by uniaxial strain tuning, Appl. Phys. Lett. **100**, 121116 (2012).

[40] H. J. Carmichael, *Statistical Methods in Quantum Optics 1: Master Equations and Fokker-Planck Equations*, Vol. 1 (Springer Science & Business Media, New York, 1999).

[41] J. R. Johansson, P. D. Nation, and F. Nori, Qutip: An open-source PYTHON framework for the dynamics of open quantum systems, Comput. Phys. Commun. **183**, 1760 (2012).

[42] A. Majumdar, P. Kaer, M. Bajcsy, E. D. Kim, K. G. Lagoudakis, A. Rundquist, and J. Vučković, Proposed coupling of an electron spin in a semiconductor quantum dot to a nanosize optical cavity, Phys. Rev. Lett. **111**, 027402 (2013).

[43] V. Loo, L. Lanco, O. Krebs, P. Senellart, and P. Voisin, Single-shot initialization of electron spin in a quantum dot using a short optical pulse, Phys. Rev. B **83**, 033301 (2011).

[44] A. Gilchrist, N. K. Langford, and M. A. Nielsen, Distance measures to compare real and ideal quantum processes, Phys. Rev. A **71**, 062310 (2005).

[45] E. Paspalakis, S. E. Economou, and F. Carreño, Adiabatically preparing quantum dot spin states in the Voigt geometry, J. Appl. Phys. **125**, 024305 (2019).

[46] B. D. Gerardot, D. Brunner, P. A. Dalgarno, P. Öhberg, S. Seidl, M. Kroner, K. Karrai, N. G. Stoltz, P. M. Petroff, and R. J. Warburton, Optical pumping of a single hole spin in a quantum dot, Nature (London) **451**, 441 (2008).

[47] D. Stefanatos, N. Iliopoulos, V. Karanikolas, and E. Paspalakis, Adiabatic control of quantum dot spin in the voigt geometry with optical pulses, WSEAS Transact. Syst. Control **14**, 319 (2019).

[48] P. Kumar and T. Nakajima, Fast and high-fidelity optical initialization of spin state of an electron in a semiconductor quantum dot using light-hole-trion states, Opt. Commun. **370**, 103 (2016).

[49] In the CW driving regime, the two driving regimes are unitarily equivalent.

[50] We use a 35 ns readout pulse as a compromise to maximize the readout fidelity across a range of cavity parameters.

[51] T. G. Tiecke, K. P. Nayak, J. D. Thompson, T. Peyronel, N. P. de Leon, V. Vuletić, and M. D. Lukin, Efficient fiber-optical interface for nanophotonic devices, Optica **2**, 70 (2015).

[52] R. S. Daveau, K. C. Balram, T. Pregnolato, J. Liu, E. H. Lee, J. D. Song, V. Verma, R. Mirin, S. W. Nam, L. Midolo, S. Stobbe, K. Srinivasan, and P. Lodahl, Efficient fiber-coupled single-photon source based on quantum dots in a photonic-crystal waveguide, Optica **4**, 178 (2017).

[53] T. Volz, A. Reinhard, M. Winger, A. Badolato, K. J. Hennessy, E. L. Hu, and A. Imamoğlu, Ultrafast all-optical switching by single photons, Nat. Photon. **6**, 605 (2012).

[54] K. Kuruma, Y. Ota, M. Kakuda, S. Iwamoto, and Y. Arakawa, Time-resolved vacuum Rabi oscillations in a quantum-dot–nanocavity system, Phys. Rev. B **97**, 235448 (2018).

[55] K. Kuruma, Y. Ota, M. Kakuda, S. Iwamoto, and Y. Arakawa, Surface-passivated high-Q GaAs photonic crystal nanocavity with quantum dots, APL Photon. **5**, 046106 (2020).